Solar Energy Materials and Solar Cells 186 (2018) 217–226

Contents lists available at ScienceDirect

Solar Energy Materials and Solar Cells

journal homepage: www.elsevier.com/locate/solmat

Efficiency limiting crystal defects in monocrystalline silicon and their characterization in production

Ferenc Korsós[a,*], László Roszol[a], Frederic Jay[a], Jordi Veirman[b], Abdelkarim Derbouz Draoua[b], Mickael Albaric[b], Tamás Szarvas[a], Zoltán Kiss[a], Attila Szabó[a], István Soczó[a], György Nádudvari[a], Nicolas Laurent[a]

[a] Semilab Co. Ltd., 2 Prielle K. str., 1117 Budapest, Hungary
[b] Univ Grenoble Alpes, CEA, LITEN, DTS, SMCP, INES, F-38000 Grenoble, France

ARTICLE INFO

Keywords:
Czochralski
Bulk micro defects
Thermal history
Light scattering tomography
PERT solar cells
Carrier lifetime

ABSTRACT

Wafers and thicker slices of an entire n-type monocrystalline silicon ingot were studied using production-compatible electrical and optical characterization techniques. We investigated the capability of these techniques to detect efficiency limiting factors in the early phase of solar cell manufacturing. In addition to the standard characterization methods and parameters - carrier lifetime, resistivity, FTIR, photoluminescence (PL) - the OxyMap technique was used to evaluate the thermal history of the wafers, while the distribution of Bulk Micro Defects (BMD) was measured using Light Scattering Tomography (LST). PERT cells and samples with amorphous silicon surface passivation – deposited at low temperature – were produced from neighboring wafers to correlate silicon properties and solar cell efficiency results.

An interesting indirect correlation was found between "as-grown" lifetime and cell performance, as both are influenced by the thermal history of the wafer.

We also observed a very strong correlation between BMD position, measured by LST on as-grown samples, and defective areas on PERT cells localized by PL measurements. The LST measurements on heat treated samples (simulating the PERT cell process) showed the growth of BMDs in low efficiency areas. It indicates that the detection of harmful defects is possible even in the as-grown material using LST technique.

1. Introduction

Modern n-type silicon cell structures show the highest stabilized efficiency in mass production, which is around 22–22.5% in today's state-of-the-art production lines. A continuously increasing market share of both homo- and heterojunction n-type cell concepts is predicted [1]. To achieve the expected efficiency improvement, recombination currents need to be further reduced in industrial scale. One key factor is the stable high-quality, high volume, cost-effective production of n-type Czochralski silicon (Cz-Si) ingots, which is supported by the generally less harmful nature of metallic impurities in n-type Si compared to p-type Si [2].

The higher crystal pulling speed – applied for the Cz-Si crystallization processes in PV industry – improves the yield of the ingot production. On the other hand, the Si ingots are grown in vacancy-rich regime [3], which can be the origin of defect generation. In addition to the formation of voids in the 1000–1100 °C temperature range during the cooling of the crystal, the formation of oxide precipitates is a significant mechanism at slightly lower temperatures [4] due to the high degree of the Oxygen supersaturation, which results in an increased total density of bulk micro defects (BMD).

Based on Voronkov's theory [5], the distribution of vacancies and Si self-interstitials are determined by the pulling conditions (v/G, where v denotes the pulling speed and G the axial temperature gradient near the crystallization front). However, the size and distribution of the grown-in BMDs is a function of the thermal history of the growing process [3,6] influenced by a several additional parameters, such as the thermo-mechanical stress during the crystallization, and concentration of dopants and other impurities (C, Ni, metallic impurities) [3,7,8].

For Cz-Si based solar cells, SiO_2 precipitation may cause a significant degradation in bulk carrier lifetime, which leads to a reduction in cell efficiency up to 4% absolute [9,10]. Therefore, it would be favorable to detect BMDs (or corresponding nuclei) – not yet being harmful but prone to growth during subsequent process – in early phase of the production. However, as it is shown in the well-known work of Haunschild et al. [11], such detection in as-cut wafers faces difficulties.

* Corresponding author.
E-mail address: ferenc.korsos@semilab.hu (F. Korsós).

https://doi.org/10.1016/j.solmat.2018.06.030
Received 17 March 2018; Received in revised form 6 June 2018; Accepted 14 June 2018
Available online 06 July 2018

Namely, the observed ring patterns in photoluminescence (PL) images – caused by the variation of effective doping level - does not necessarily reflect/indicate reduced carrier lifetime in the finished homojunction cell.

For the crystalline / hydrogenated amorphous silicon (c-Si/a-Si:H) heterojunction solar cells (HJT) – using only low temperature manufacturing process steps – the efficiency of the finished cells can be predicted from *as-grown* bulk carrier lifetime and the bulk resistivity [12,24]. In some particularly defective Cz-Si wafers however, the knowledge of the as-cut lifetime may not be enough to predict the cell efficiency due to the formation of a light-induced defect upon illumination of the cell [13].

So far, the manufacturing of all types of homojunction cell structures includes high temperature process steps in the 800–1000 °C temperature range. During the diffusion or annealing processes, the nuclei formed during the crystallization grow further resulting in larger BMDs. Such precipitation may reduce the carrier lifetime, and consequently degrade the cell efficiency. Under industrial Cz-Si pulling conditions, wafers from the upper tens of centimeters of the ingot at the seed part is exposed to this precipitation phenomenon [6,14] if the pulling process is not controlled carefully.

Since these efficiency-limiting defects are generated during solar cell processing, their inspection in the as-grown crystal is problematic even by measuring the bulk lifetime [8,14], as their nuclei may simply show no recombination-activity.

One possible solution for such inspection is to apply the relationship between the thermal history and the final cell efficiency. It is shown in [6] that high Thermal History Index (THI) measured using the "OxyMap" technique [15] predicts the appearance of the ring pattern defects which reduce cell efficiency if the interstitial oxygen concentration [O_i] is sufficiently high.

Carrier lifetime (LT) and especially photoluminescence (PL) measurement methods are known to be efficient techniques characterizing the electrical quality of the Si samples at every stage of the PV cell production chain [16–18]. Size and distribution of microdefects are mostly characterized by optical microscopy after chemical defect etching. In the semiconductor IC industry – where the BMD size and density distribution are also important material parameters – Light Scattering Tomography (LST) is a known and accepted characterization technique, which is mostly used to inspect the quality of the defect-free denuded zone at the wafer surface [19].

In this work, we investigate the capability of the LST technique to detect BMDs in thick slices from as-grown crystal and try to confirm their detrimental impact on the solar cells efficiency.

2. Experimental

2.1. Sample preparation

A 90 kg phosphorus-doped Cz-Si ingot was crystallized, with an average pulling speed of ~ 36 mm/h. After squaring, the ingots were cut into four bricks (B1-B4). For FTIR and BMD characterization, 1 mm thick slices were cut from the ends of each brick (see Fig. 1).

After performing the relevant brick-level characterization, the bricks were sliced into wafers using the diamond wire sawing technique. Neighboring wafers were used for as-cut wafer characterization, for symmetrical intrinsic /n-doped (i/n) a-Si:H passivation stacks [12] and to manufacture PERT (Passivated Emitter Rear Totally diffused) cells at CEA-INES (details and the process flow are described in [20]). Around 40 solar cells and 40–40 as-cut and passivated wafers were fabricated for the study. The scheme of the performed measurements is summarized in Fig. 2. After the initial BMD characterization performed on the thick slices by LST, the samples were heat treated in two steps intended to mimic the PERT processing (within the 800–1000 °C range) and re-measured thereafter.

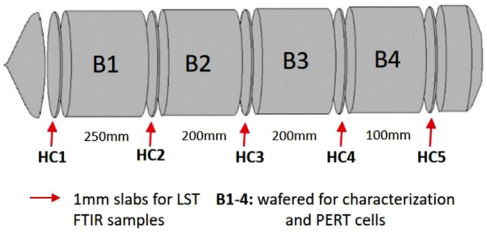

Fig. 1. Illustration of the ingot used for the study. 1 mm thick slices were cut from the end of each ingot part for FTIR and BMD characterization. Neighboring wafers from the four sections covering the entire length of the ingot were used for as-cut characterization, surface passivation and PERT cells.

2.2. Characterization techniques

In this work, the application of industrial-compatible, preferably non-contact measurement methods are studied. The characterization techniques and systems used for this study are listed below.

2.2.1. Resistivity

Resistivity (ρ) testing was performed on samples of all geometry types (bricks, thick slices, and as-cut wafers) using an eddy-current sensor. Resistivity measurement is available in different tools used for this study. The resistivity values determined by the different systems on all sample types were within 10% for the same part of the ingot. ρ values required for implied V_{oc}, (i-V_{oc}), [TD] and THI calculation were obtained using an OxyMap system from AET Solar Tech. Not to confuse the reader, we made the choice to only show results from the OxyMap system.

2.2.2. Carrier lifetime

Depending on the sample type and the distribution of the work for this study, carrier lifetime was tested using different measurement techniques and systems.

- Eddy-current PCD (e-PCD) technique [21] was applied for bulk lifetime measurements on the bricks using a Semilab WT-2000DI system.
- μ-PCD technique of Semilab WT-2000PVN system was used for effective lifetime (τ_{eff}) mapping in passivated samples.
- QSS- μPCD carrier lifetime measurements [22] were performed on the passivated wafers determine the carrier lifetime at given injection levels.
- τ_{eff} and i-V_{oc} values were obtained using the QSS-PC technique using a Sinton WCT-120 system at CEA- INES on PERT cell precursors (before metallization).

2.2.3. [TD], Thermal History Index

Determined by the OxyMap technique [15]. The method is based ρ measurements at as-grown state (ρ_1), after 450 °C TD generation annealing process (ρ_2), and finally after a TD killing annealing at 700 °C (ρ_3). Doping concentration, as-grown [TD], [O_i] and THI are calculated from these three ρ values. THI can be applied as an indicator of the cooling velocity of the material during the pulling process [6].

2.2.4. Quasi-Steady-State PL (QSS-PL) for passivated samples

PL images were captured using the on-the-fly PL imaging capability of the Semilab PLI-1001B system. For the proper in-line acquisition of PL images of passivated samples, the sample is illuminated in a wide stripe (perpendicular to transport direction), which ensures the steady-state conditions [17,18], while the PL photons are captures using a suitable CCD camera equipped with optimized optics.

Using similar optical arrangement, PL images of the bricks were recorded by a Semilab PLB-55 equipment.

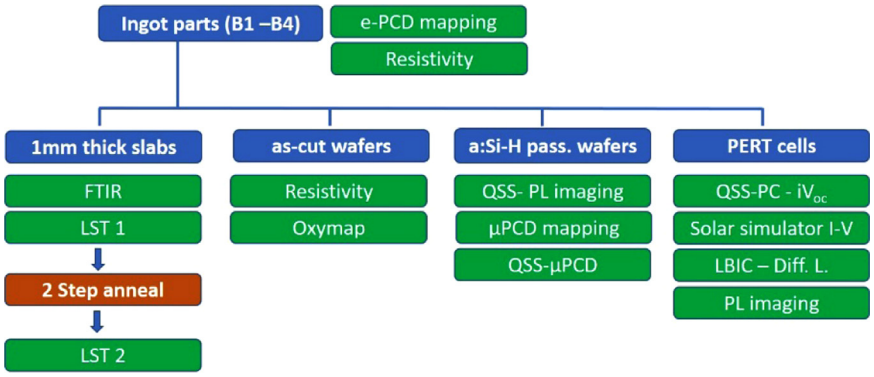

Fig. 2. Scheme of the performed measurements. To evaluate the PERT cell properties, QSS-PC-iV$_{oc}$ measurements were performed on the cell precursors, after the ARC layer deposition, while the other techniques (I-V, LBIC, PL) were applied after the metallization.

2.2.5. Light Scattering Tomography (LST)

For the LST measurements the 1 mm slices (HC1-HC5) with polished surface were cleaved diagonally. During the measurement, the infrared laser light is focused to the front side surface of the sample close to the cleaved edge, while the photons originated from the Rayleigh scattering on the BMDs are captured by a CCD camera from the side of the cleaved edge. By moving the sample, the full image of the scattering objects in the depth range – equivalent to the laser spot size – is recorded. The detected scattered intensity strongly depends on the BMD size, d ($I_{scatt} \sim d^6$). Thus, depending on the image capturing parameters, defects in different size ranges are detected: 20–45 nm (small size), 40–80 nm (medium size), 70–140 nm (large size). In crystal defect science, Light Scattering Tomography Defect (LTDS) is the dedicated name for any defects detectable by LST technique. However, in the present work, the term "BMD" is used for such defects. One recorded image corresponds to 2 mm length along the edge. The number of light scattering objects detected within one image is converted to BMD density. These BMD density values are plotted in the graphs of the radial BMD distribution.

3. Results and discussion

3.1. Resistivity, [Oi], Doping, [TD]

Fig. 3a shows [O$_i$] values at different ingot heights obtained by Fourier-Transform Infrared spectroscopy (FTIR) measurement according to SEMI MF1188 standard. Going from the seed to the tail of the ingot [O$_i$] decreases by 30% from the maximum value of 1.07 × 10^{18} cm^{-3}. The variation of the as-grown ρ along the ingot is visible in Fig. 3b (blue dots). This ρ is the result of the addition of two dopants: Phosphorus which is intentionally added to obtain targeted ρ and TDs which are generated during the ingot crystallization at the cooldown step. Green dots in the Fig. 3b represents [TD] along the ingot center and red dots ρ after TD killing. The high amount of TD in the seed part of the ingot is responsible of the high ρ difference between as-grown and TD killing states. It is important to notice that as-grown TDs are killed during the PERT solar cell process. These ρ values are used to calculate the variation of THI along the ingot in Section 3.4.

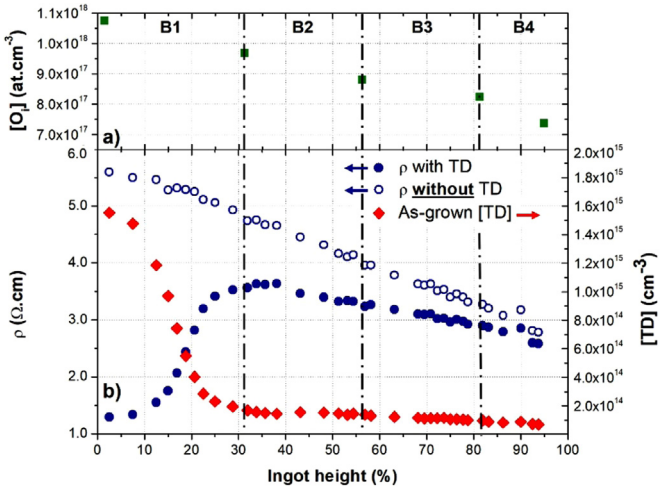

Fig. 3. a) FTIR [Oi] results show ~ 30% decrease of [O$_i$] from top to tail along the ingot. The as-grown ρ profile along the ingot shows the [TD] dominated initial increasing section followed by the slow decrease due to P segregation. b). [TD] values are calculated from ρ measurements before and after TD killing anneal.

3.2. n-PERT cell results

Solar cells were characterized using a solar simulator under standard test conditions (STC: AM1.5 spectrum, 25 °C, 1000 W/m^2). As shown in the Fig. 4, the conversion efficiency rises from the ~ 18.5% measured in cells using wafers from the top-seed part of ingots (first values in B1 ingot section in Fig. 4) to slightly above 20%, for those from the bottom-tail part (B2-B4 ingot sections). The efficiency is mainly driven by the Open Circuit Voltage (V$_{oc}$), which shows an improvement of 30 mV, from 615 mV to 645 mV. It can be noticed, that the Fill Factor (FF) and J$_{sc}$ also varied but with lower amplitude. The stabilization of the V$_{oc}$ values after 30% of the ingot height indicates that the cell efficiency is mainly limited by the PERT processing/structure for middle/tail part of the ingot. The wafer bulk properties had no impact on the solar cells performance for 70% of the ingot, which is confirmed by the considerably larger implied V$_{oc}$ in the high

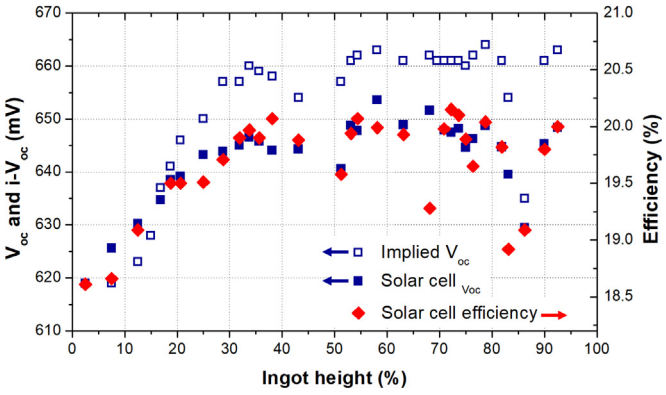

Fig. 4. Cell efficiency (a), Voc and i-V$_{oc}$ (b) measured on the cells plotted against the corresponding wafer position in the ingot. The ~ 10 mV larger i-V$_{oc}$ compared to V$_{oc}$, that the efficiency is limited by cell processing, and not by bulk material quality.

Table 1
Ranges of the main material and cells parameters related to the samples from the entire ingot.

ρ [Ω cm] (with TD)	ρ [Ω cm] (without TD)	P doping [E14 cm^{-3}]	[O_i] [E17 cm^{-3}]	[TD] [E14 cm^{-3}]	η [%] PERT	FF	Voc [mV]	i-Voc [mV]
1.2–3.0	5.5–2.8	8–18	7–11	0.7–15	18.5–20.2	77–80	615–650	620–665

efficiency part (up to 663 mV) as well. The difference between i-V_{oc} and V_{oc} after 25–30% of the ingot height is due to the recombination at the metallic contacts.

Therefore, as i-V_{oc} reflects the changes in bulk quality with larger sensitivity, hereinafter this parameter is used in comparative graphs. The dip of solar cell performance parameters in the B4 part is likely caused by contamination from the boat during the wet chemical or diffusion processes, and not by as-grown material properties. The representative material and cell parameters are summarized in Table 1.

3.3. "As-grown" carrier lifetime measurements on ingots and passivated samples

It is generally accepted that thermal processes under 250 °C do not change the properties of BMDs, therefore a-Si:H, deposited by PE-CVD at such low temperatures, are used as passivation layers. Furthermore, the (i/n) a-Si:H stacks deposited on the wafer surface provide excellent surface passivation (surface recombination velocity, SRV: < 1 cm/s) [13]. For carrier lifetime measurements on such passivated samples, τ_{eff} are very close to the bulk carrier lifetimes of as-grown crystals up to 5–10 ms.

PL imaging, eddy-current PCD technique [21], or other PCD methods are also applicable to characterize bulk recombination properties directly on the as-grown crystal, although their proper evaluation is less straightforward compared to probing carrier lifetime on the passivated wafer (τ_{pass}).

As it is shown in [14], reduced carrier lifetime in the P-band can be observed even in the as-grown crystal. The P-band is located at the boundary of the vacancy and intestinal rich areas in wafers, if [O_i] is sufficient and crystal growth is slow enough (P-band position is governed by v/G). Thus, the P-band mostly exists in wafers from the top part of the ingots, where the pulling speed is lower during the crystal growth.

During subsequent high temperature heat treatments, oxide precipitates - already present in the P-band – grow and induce stacking faults (Oxidation Induced Stacking Fault, OSF) forming the so-called OSF rings.

Due to the relatively slow pulling speed used during the manufacturing of our bricks, the P-band can be observed even in the second ingot section (B2). In Fig. 5 it is demonstrated that if the P-band ring diameter exceeds the square wafer size, the P-band defects are detected also on the PL images and e-PCD maps recorded on the brick side. The concurrence of patterns observed in PL images and μPCD maps confirms that the band pattern is related to defects, and not the result of doping variations.

τ_{pass} and e-PCD lifetime readings are close to each other under 4 ms, where surface recombination starts to dominate over the bulk lifetime in the passivated wafers. Therefore, it appears that the combination of PL and e-PCD measurement performed on the cut face of the brick is capable to determine the geometrical parameters of the P-band and the bulk lifetime in the seed-end region.

3.4. Relationship of as-grown lifetime and cell performance

As it was shown in the previous section, the as-grown carrier lifetime can be determined on the bricks e.g. using e-PCD technique. In our project, we investigated the as-grown lifetime using τ_{pass} results from the passivated wafers providing more detailed insight to the as-grown material properties. In this section, we analyze the possible application of as-grown lifetime measurements to predict the cell efficiency.

Defects might be formed during the homojunction solar cell processing [8,11] causing carrier lifetime degradation and so loss in cell performance. Thus, carrier lifetime in the as-grown material does not necessarily directly predict the efficiency of finished homojunction cell. Carrier lifetime in n-type mono materials is ranging from several hundreds of microseconds, from 900 μs in our ingot (Table 2, Fig. 6/a). Bulk carrier lifetime above 900 μs does not limit the lifetime in the 20% efficiency range or below. This suggests that – indeed – the material degradation during the cell processing is responsible for the lower efficiency of the cells from the first 30–40% of the ingot height (see Fig. 4), and the as-grown lifetime itself is not the responsible factor for the lower efficiency.

Nevertheless, in Fig. 6/a one can observe a surprising match in the trends of i-V_{oc} and $log_{10}(\tau_{pass})$ values, especially in the first 40% of the ingot height.

The observed good correlation between the as-grown lifetime and cell performance has an indirect nature. In the understanding of this relationship, the thermal history of the wafers plays the key role.

I. From one side, if both [O_i] and THI are high, the wafer is prone to the formation of oxide related defects during the subsequent PERT processing [6]. Thus, cell performance is supposed to correlate to some combination of [O_i] and THI, if the oxide related defects are the dominant efficiency reducing factors. This presumption is confirmed in Fig. 6/b, where i-V_{oc} is compared to $([O_i] \times THI)^{-1}$ along the ingot.

II. From the other side, again high [O_i] and high THI results in larger thermal donor concentration. In Fig. 3. it was shown how [TD] decays along the ingot due to the decreasing THI. However, although the recombination activity of thermal donors is weak, at high [TD] levels they cause significant recombination [23]. So, TDs might be responsible for the lower as-grown lifetime for samples from the seed-end part.

To check this assumption, we compared the τ_{pass} values (representing as-grown lifetime) to carrier lifetime values extracted from [23] (Fig. 7). In the experiments of Tomassini et al. [23], [TD] was intentionally adjusted by thermal annealing. Nevertheless, τ_{pass} values we obtained on the passivated samples are within 15% to the lifetime values reported in their work in the overlapping [TD] interval.

It confirms that the carrier lifetime in the as-grown crystal is dominated by recombination at TDs. In summary, both the cell performance and the as-grown carrier lifetime are impacted by thermal history and [O_i] in similar but independent ways, causing the apparent correlation between them.

It should be noted, that in Fig. 7. the plot of the τ_{pass}^{-1} values against [TD] exhibits a quite linear relationship for [TD] levels above 3×10^{14} cm^{-3}, and a deflection from the linear trend below this threshold. This unexpected deflection is not related to surface passivation, but it comes from the unique recombination properties of TDs. The faster reduction of the lifetime at high [TD] levels comes from both the increase of carrier cross section and ρ reduction, if modelling the recombination processes according to single level Shockley-Read-Hall model. Further details concerning the SRH parameterization of TD related recombination can be found in [23].

In conclusion, the measurement of the as-grown bulk lifetime in good quality n-type ingot indicates the material's susceptibility to

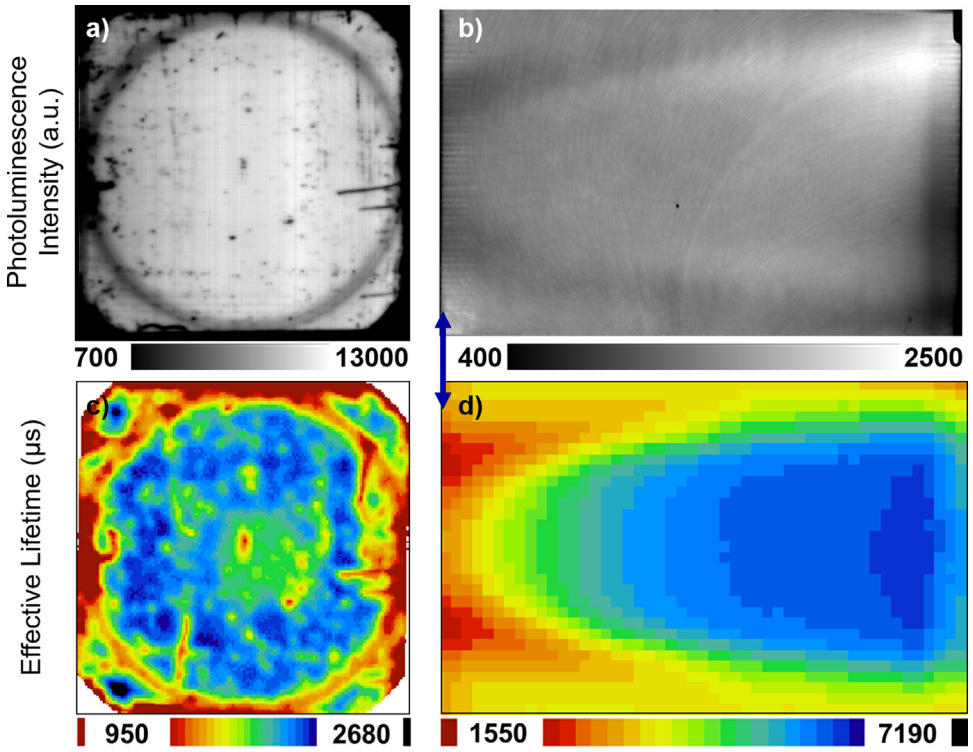

Fig. 5. a) and c) show, respectively, the PL image and the µ-PCD map of the last passivated wafer of the B1 brick. b) and d) are, respectively, PL image and e-PCD map of brick B2. Blue arrows indicate that the passivated wafers are originated from the ingot position close to the edge of the measured brick. The color scale is adapted to show the P-band circle signatures. The trace of the P-band is detected both in the PL image and e-PCD map of the same brick side. (For interpretation of the references to color in this figure legend, the reader is referred to the web version of this article.).

Table 2
Range of the carrier lifetime values in the amorphous Si passivated samples and in the PERT cell precursor samples, measured by QSS-PCD.

As-grown carrier lifetime in a-Si:H pass. wafers	Carrier lifetime in cell precursors
900–6000 µs	70–310 µs

process induced BMD formation in an indirect way.

THI can be calculated from [TD] and [O_i] [6]. [TD] can be estimated applying resistivity measurement, and using experimental or modelled P doping level, while [O_i] is usually acquired by FTIR even in production.

Thus, for industrial applications, the measurement of as-grown lifetime (for instance e-PCD measurement on ingots) can complete the material quality test routine, providing more accurate prediction of the expected cell efficiency. To specify the proper way how to apply these three as-grown material parameters requires further studies on extended range of material properties.

In the tested ingot the as-grown lifetime is dominated by TDs. It is possible that the recombination on TDs hides a less recombinative process related to defects already exist in the as-grown material, causing the observed degradation during the cell processing. This can be checked by applying TD killing anneal prior to the amorphous silicon passivation on a similar sample set.

3.5. Process induced defects in PERT cells

As it was shown in Section 3.3, in PL images of passivated wafers only the P-ring related defects are visible. In Fig. 8, the comparison of the PL images recorded on an a-Si:H passivated sample and on the PERT cell fabricated from the neighboring wafer – all coming from the middle of the seed-top B1 brick - leads to the following comments:

- While only the P-band appears in the PL image of the passivated sample, reduced lifetime area is observed in the center of the PERT cell. Diffusion length measurement by LBIC method (using Semilab WT-2000PVN system) confirms that the black circle pattern in the PL image corresponds to degraded bulk lifetime.
- The reduced lifetime area is delimitated by the original radius of the P-band's inner boundary.
- The P-band is not visible in PL image of PERT cell.
- On the PERT cell, we can observe defects not related to the bulk material: scratches due manual handling and a dark stripe

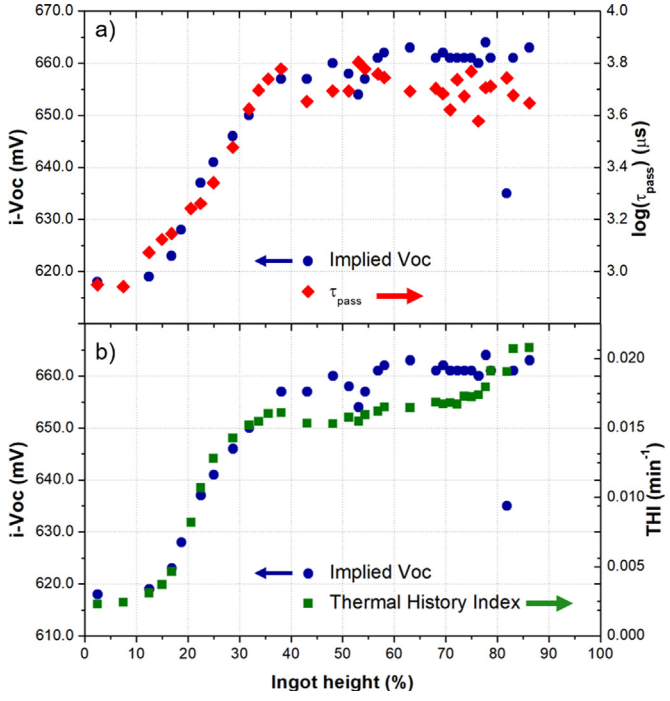

Fig. 6. Relationship between a) as-grown lifetime, b) [O_i]xTHI, and i-V_{oc}. The logarithm of τ_{pass} measured by QSS-µPCD at 1×10^{15} cm^{-3} injection level (a) and the inverse of [O_i]×THI (b) follow the same trend as i-V_{oc}. Scales are adapted to visualize the correlations.

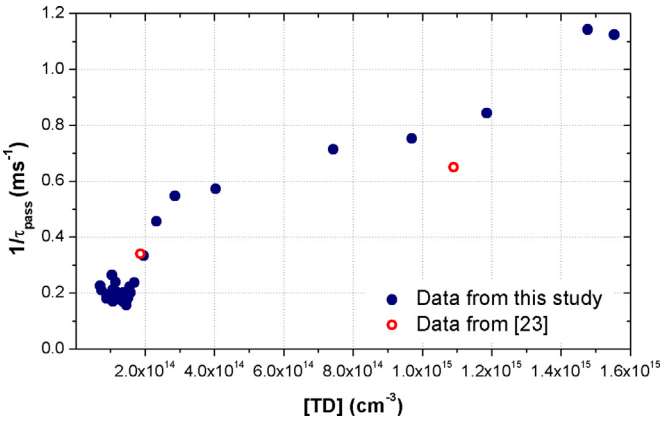

Fig. 7. The $1/\tau_{pass}$ vs. [TD] plot shows a linear relationship above 3.10^{14} cm^{-3} [TD] and a deflection from this linear trend below this threshold. The scatter in the initial part is caused by the variation of the passivation quality. Both the lifetime values and the shape of the curve agrees with the findings of the experiments of Tomassini et al. [23].

originated from the metallization process.

Based on the μ-PCD mapping of the passivated sample (not presented), the bulk carrier lifetime in the P-band area is above 600 μs even in the lowest lifetime a-Si:H passivated samples. In all PERT cell precursors, the carrier lifetime was below 310 μs (see Table 2). Thus, the disappearance of the P-Band does not necessarily means that defects are "recovering", instead, merely the process induced lifetime degradation is more significant in surrounding area. It is especially pronounced inside the black ring.

It indicates that the BMD formation during the high temperature process steps of the PERT cell production is related to vacancies, or vacancy related aggregates. The resulted BMDs are generally accepted to be oxide precipitates [8,11,14].

3.6. Detection of BMDs by Light Scattering Tomography

Formation of oxide precipitates are generally supposed to be responsible for the reduction of lifetime during high temperature processing steps. However, $[O_i]$ does not change considerably within the entire crystal (see Fig. 3/a). Small aggregates or BMDs may act as nuclei for inducing precipitations during the PERT process.

LST can detect crystal defects above ~15 nm size, and above 3×10^5 cm^{-3} density in a non-contact, non-destructive way. Therefore, evolution of BMDs during anneal can be monitored in the same sample piece. The depth (from the cleaved edge face) in which BMDs are detected is roughly 10 μm with our measuring setup.

By applying different laser intensities for the LST measurement, defects in different size ranges are detected. The measuring recipes were optimized for three BMD size ranges: small [20–45 nm] – blue curve in stats, medium [40–80 nm] – orange curve, large [70–140 nm] – green curve.

We compared LST images, statistical results in the as-grown slices, and in the same slices after the PERT process equivalent thermal anneal. Examples of the captured LST images – at 20 mm radial position in HC1 slice – by different settings are depicted in Fig. 9. It demonstrates the typical features visible in the LST images.

Large size BMDs were not detected in the as-grown thick slices but observed in the LST image after anneal. Large BMDs appear as extended saturated spots in LST images recorded using the recipe for the medium size defects (Fig. 9/b). Image of small size BMDs suffers from this phenomenon even more. The signal saturated spots can be as large to hide the signal coming from smaller precipitates. Thus, if significant number of large defects exists in the sample, small BMDs may not be reliably detected. For such samples the density of the small BMDs, therefore, is not presented in the radial BMD distribution plots. Since large BMDs were not detected in the as-grown slices, the corresponding measurements are also omitted in the graphs.

In the image of the large BMDs, groups of defects appear (marked as multiple BMDs in Fig. 9/c). Their arrangement seems to follow crystallographic axes. Their emergence is probably related to the stress field introduced by the growing precipitates. In this study, their existence is

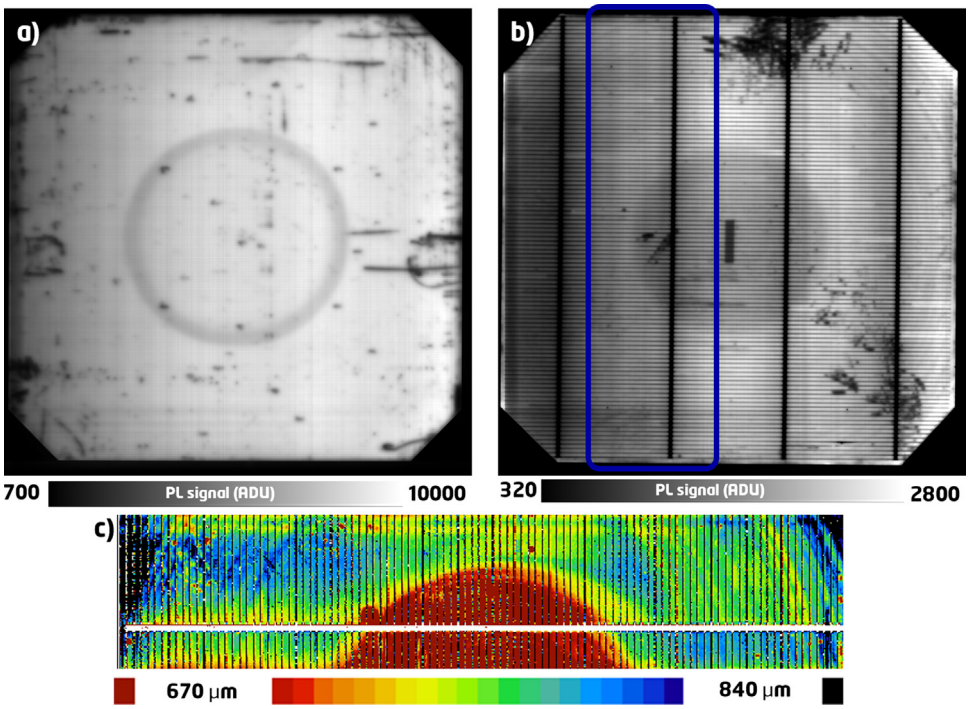

Fig. 8. a) PL images of a passivated wafer and b) the PERT cell fabricated from the neighboring wafer in the middle of B1 brick. The observed disk pattern inside the P-band corresponds to reduced bulk lifetime. c)It is confirmed by LBIC diffusion length measurement.

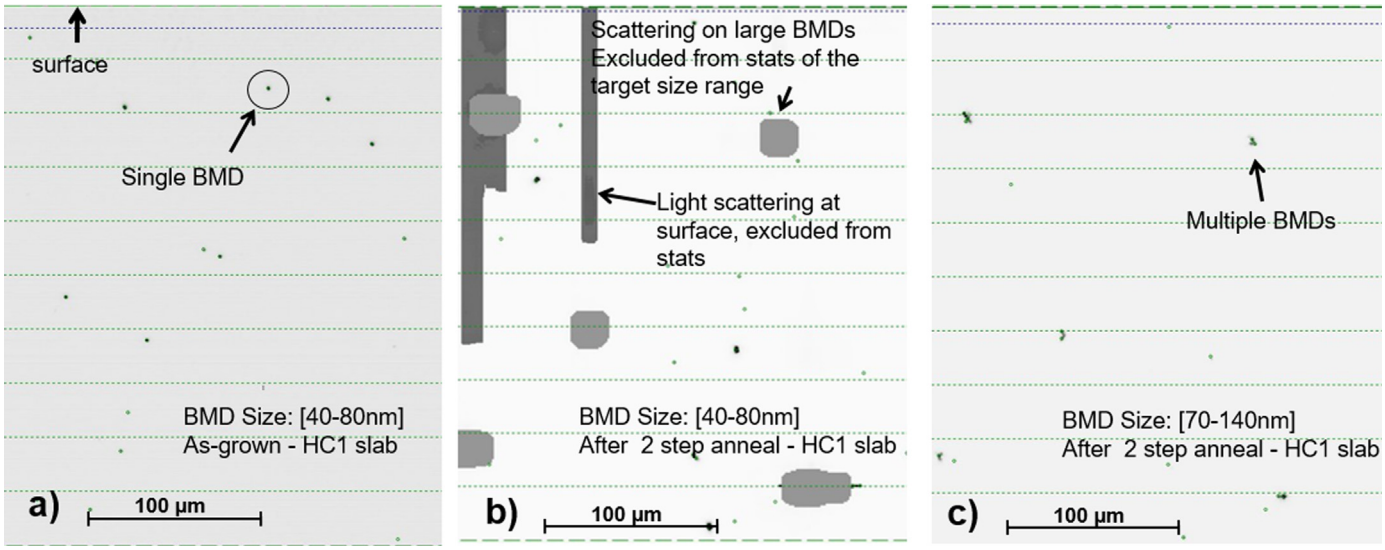

Fig. 9. Examples of LST measurements of slice HC1 before (a) and after (b, c) heat treatment and using different recipes for the detection of medium (a,b) and large (c) size defects in the same position along the cleaved edge of the slice. The images demonstrate the typical features visible in the LST images as well. The results visualize the significant increase of BMD size. In addition, formation of large BMDs in close locations (multiple BMDs) is observed after the anneal.

only noted, but their properties are not studied in detail.

In the radial BMD distribution plots related to the ingot-top HC1 slice (Fig. 10), small and medium size BMDs are counted in the 1–5 × 10^7 cm^{-3} density range inside the P-band. The radial position of the maximum BMD density may correspond to P-band but it cannot be confirmed without any doubt. The reason for this uncertainty is the small difference in the ingot position for PL and the LST measurements. The illustrating PL images are recorded on samples at 20–25 mm distance from the slice's height position in the ingot and the diameter of the P-band ring might change considerably even within some centimetres in such early crystallized part of the ingot.

We conclude, that the size of the BMDs increased significantly while their density remained unchanged on the inside of the P-band as the result of the thermal anneal. In the outside region, large density (~ 2 × 10^8 cm^{-3}, secondary axis in the image) of small size [20–45 nm] defects evolved. Their origin and possible impact to cell performance is not yet cleared.

At the position of HC2 slice in the ingot, the related cells have not reached the maximum efficiency yet. Within the P-band, the amount of medium size defects is at the detection limit (~ 3 × 10^5 cm^{-3}), but circa 1 × 10^7 cm^{-3} density of small defects appears (Fig. 11). Large precipitates are found of the same density and distribution after the anneal. The maximum BMD position seems to be related to the P-band. The PL image of the PERT cell shows a subtle darker tone inside the OSF ring, causing a low but measurable efficiency reduction.

A graphical summary of the main results is represented in Fig. 12. The cell efficiency loss seems to correlate to the density of large size (> 70 nm) defects. The recombination rate at the oxide precipitates scales with their interfacial surface [10]. Larger precipitate means stronger recombination, and thus leads to lower conversion efficiency.

Small and medium size precipitates are found in the central area - delimited by the P-band – of the as-grown HC1 and HC2 slices. As the result of the heat treatment, enlarged precipitates are detected with the same density and distribution. This allows to pose, that the detection of these small and medium size BMDs in the as-grown crystal - together with the determination of the P-band position - can predict the evolution of the larger defects during high temperature anneals, and so the efficiency loss during homojunction cell production. Further studies on wider sample scales are needed to validate the generality of such prediction.

In the outer regions of slices HC3–5, considerable number of small BMDs are found. The density of large size defects originated from them is minimal. They do not seem to act as efficiency limiting factor, leastwise not up to 20%, what was achieved in our n-PERT cells.

4. Conclusions

In this paper, we studied the applicability of production-compatible measurement techniques for n-type wafers to predict the evolution of oxygen related defects during the PERT processing – causing low efficiency – in the early stage of the PV cell production.

Carrier lifetime maps and PL imaging visualize the P-band related ring pattern in ingots and in surface-passivated samples. However, the defects responsible for the low efficiency of cells from seed-end wafers do not appear when imaging as-grown material properties. The defects forming in the vacancy-rich regions inside the P-band of the wafer during the PERT cell processing are revealed only in the PL images recorded on the PERT cells and appear as a degraded lifetime disk in the wafer center.

An interesting correlation was found between the as-grown lifetime and the cell performance, although the defects - degrading the efficiency - form during the cell processing. High [O_i] and high Thermal History Index factor together indicates the material's susceptibility to efficiency degradation, and cause reduced as-grown lifetime in the same time due to the formation of thermal donors. TDs are eliminated during the homojunction cell processing; thus, this correlation evidently has an indirect nature.

This relationship is suggested to be applied in a combination with resistivity and [O_i] measurements to define the material's susceptibility to the formation of harmful defects.

Further tests are planned to investigate, whether lifetime measurements on samples passivated after TD killing process reveal further defects related to low efficiency cells.

Finally, the LST technique was proven to be capable to detect the presence of the main harmful defects for the solar cell efficiency in very early phase of the process flow. Significant BMD density was detected in test samples from the low efficiency part of the ingot in positions corresponding to degraded cell area, although reduced lifetime is not observed in the as-grown material and amorphous Si passivated wafers. The increase of BMD size (without change in BMD density) after PERT process equivalent anneal was also observed using the LST technique. It indicates, that given BMDs detected in the as-grown test pieces induces

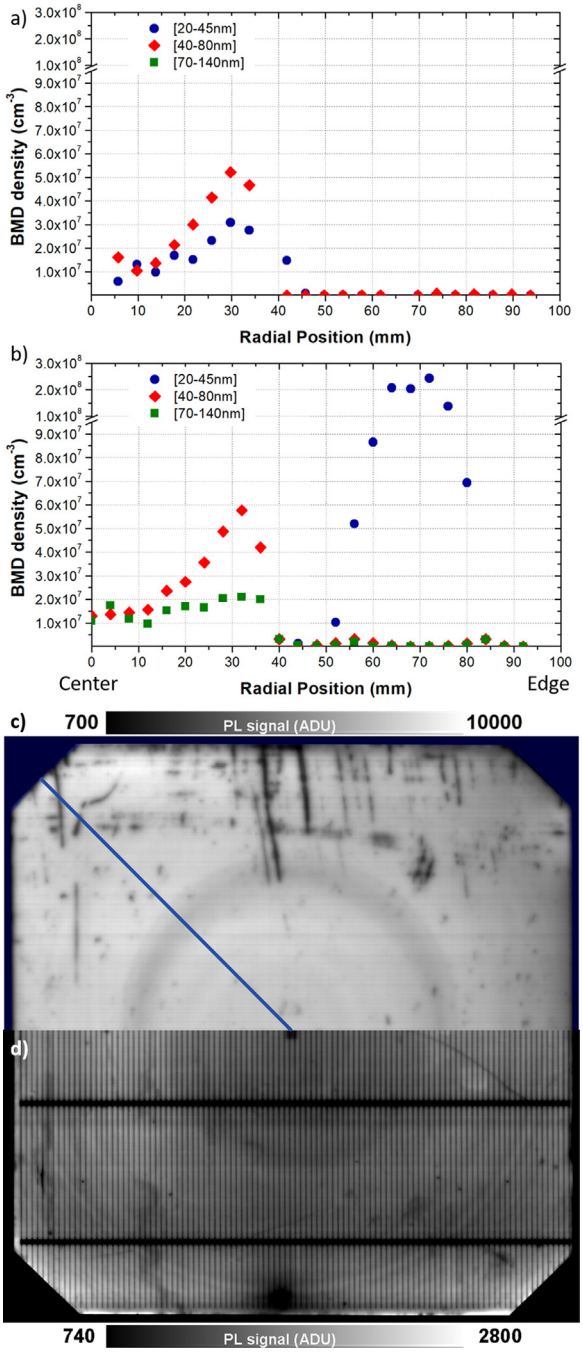

Fig. 10. Characterization of samples from the tail part of the brick 1. a) and b) represent the variation of BMD density for different BMD sizes, respectively on the as-grown sample and after annealing to simulate the PERT process, taken across the samples (blue line). c) and d) are, respectively, the PL images of the passivated sample and the finished PERT cell. (For interpretation of the references to color in this figure legend, the reader is referred to the web version of this article.).

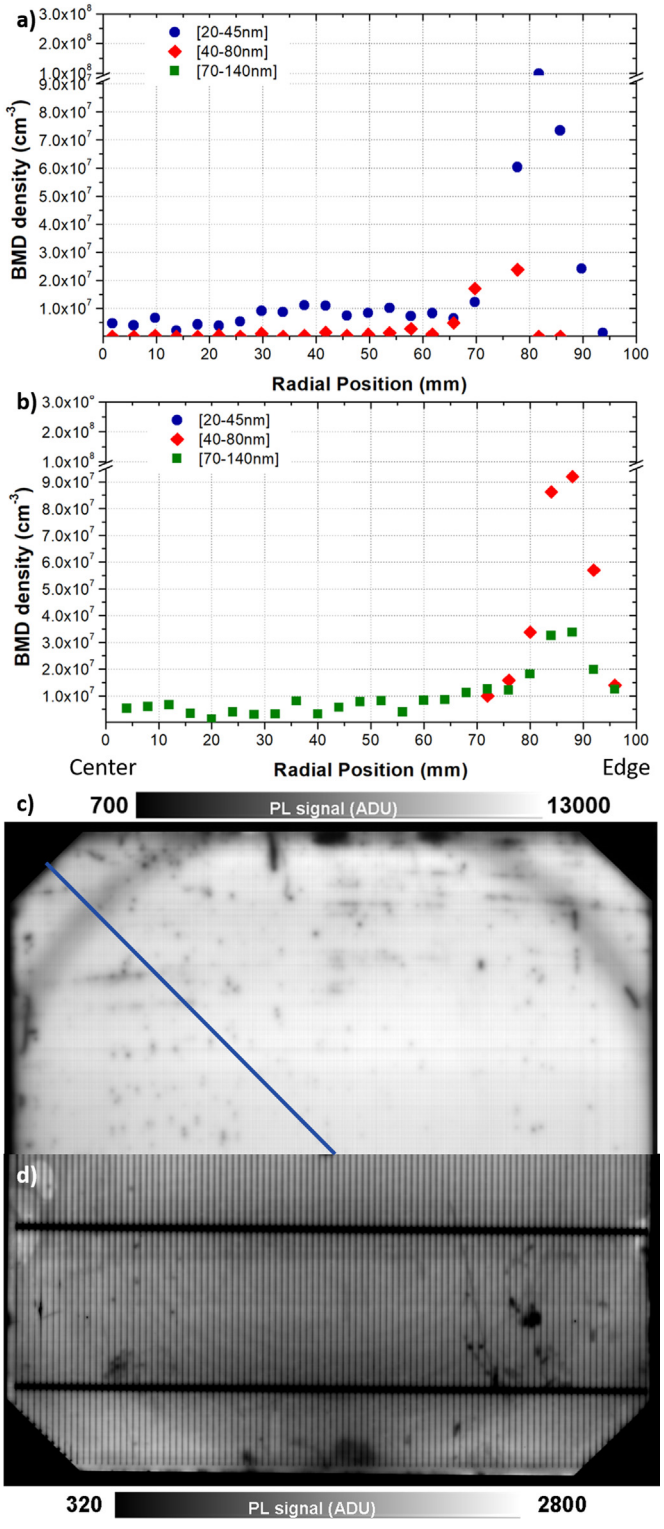

Fig. 11. Characterization of sample from the tail part of the brick 2. a) and b) represent the variation of BMD density for different size, respectively on the as-grown sample and after annealing, taken across the samples (blue line). c) and d) are, respectively, the PL images of the passivated sample and the finished PERT cell. (For interpretation of the references to color in this figure legend, the reader is referred to the web version of this article.).

degradation during the homojunction cell processing.

Thus, despite the increase of their size during the solar cell manufacturing, the defect quantities observed in the as-grown material are enough to evaluate the silicon quality and provide a very good first evaluation and selection of the monocrystalline silicon material.

Acknowledgements

This study is a joint work between Semilab Co. Ltd and French National Institute of Solar Energy (CEA-INES). All material and solar cells were provided by CEA-INES, thus OxyMap and solar cells characterization were also performed by CEA-INES. All other industrial-compatible and advanced characterizations were performed by Semilab

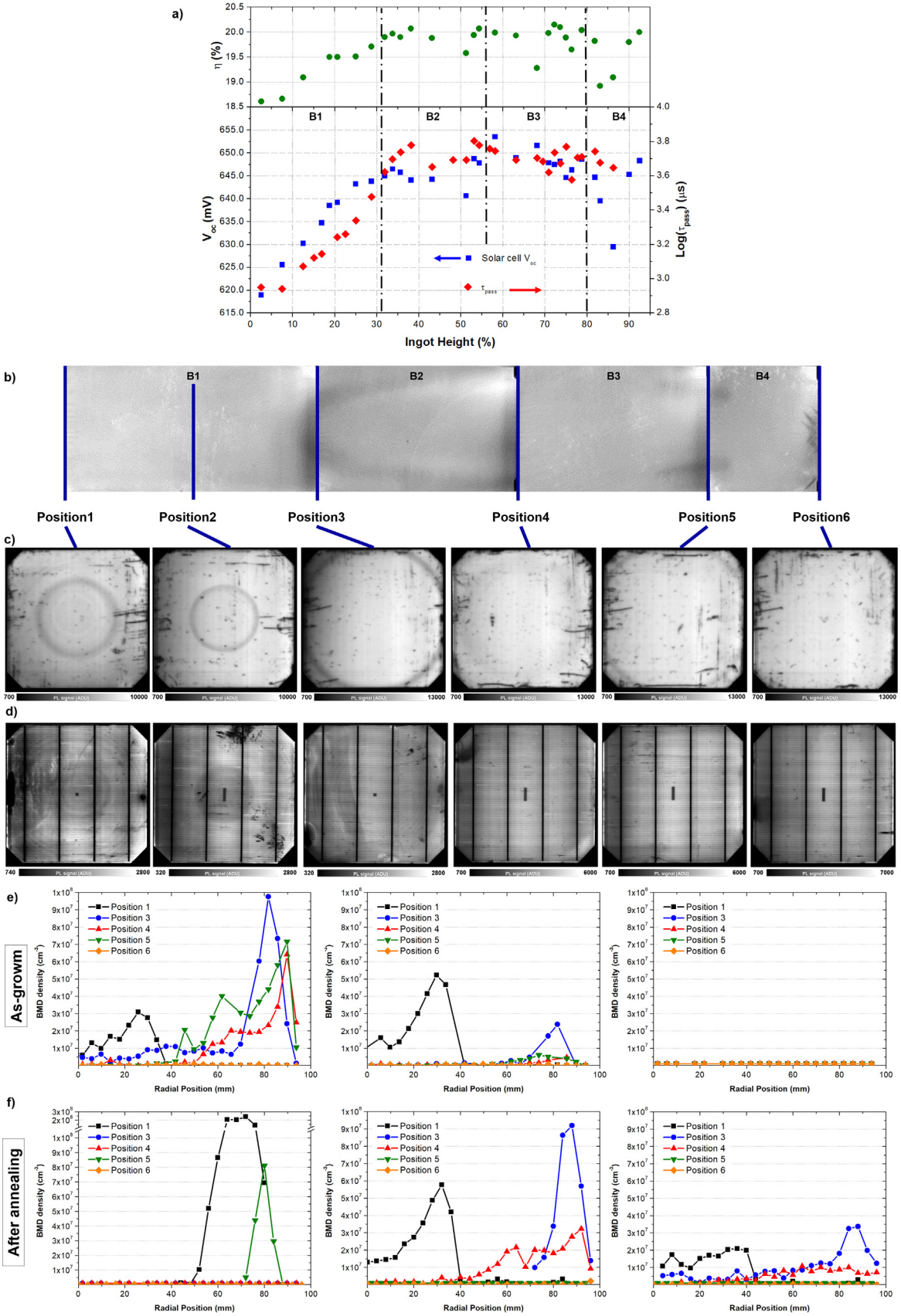

Fig. 12. Graphical summary of the results illustrating the relationship between BMDs detected by LST, the appearance of the defects in the PL images, and their impact to the cell performance. a) performance of solar cells and carrier lifetime on passivated samples, b) PL images of the ingot, c) PL measurements on passivated samples, d) PL images of PERT solar cells, e) LST results before annealing and f) after annealing.

Co. Ltd.

The authors would like to acknowledge Gábor Paráda, Zsolt Horváth and Ilias Saegh, colleagues at Semilab, for performing the μ-PCD, e-PCD and QSS- μ-PCD measurements for this study.

Appendix A. Supplementary material

Supplementary data associated with this article can be found in the online version at http://dx.doi.org/10.1016/j.solmat.2018.06.030.

References

[1] 9th edition of International Technology Roadmap for Photovoltaic (IRTPV): 2017 results, 2018.
[2] D. Macdonald, L.J. Geerligs, Recombination activity of interstitial iron and other transition metal point defects in p- and n-type crystalline silicon, Appl. Phys. Lett. 85 (2004) 4061–4063.
[3] W. Ammon, A. Sattler, G. Kissinger, Defects in Monocrystalline Silicon, Springer Handbook of Electronic and Photonic Materials, Springer, 2017, pp. 111–132.
[4] R. Falster, V.V. Voronkov, F. Quast, On the properties of the intrinsic points defects in silicon: a perspective from crystal growth and wafer processing, Phys. Status Solidi (b) 222 (2000) 219–244.
[5] V.V. Voronkov, R. Falster, Grown-in microdefects, residual vacancies and oxygen precipitation bands in Czochralski silicon, J. Cryst. Growth 204 (1999) 462–474.
[6] J. Veirman, B. Martel, E. Letty, R. Peyronnet, G. Raymond, M. Cascant, N. Enjalbert, A. Danel, T. Desrues, S. Dubois, C. Picoulet, X. Brun, P. Bonnard, Thermal history index as a bulk quality indicator for Czochralski solar wafers, Sol. Energy Mater. Sol. Cells 158 (2016) 55–59.
[7] A. Borghesi, B. Pivac, A. Sassella, A. Stella, Oxygen precipitation in silicon, J. Appl. Phys. 77 (1995) 4169–4244.
[8] G. Gaspar, G. Coletti, M. Juel, S. Würzner, R. Søndenå, M. DiSabatino, L. Arnberg, E.J. Øvrelid, Identification of defects causing performance degradation of high temperature n-type Czochralski silicon bifacial solar cells, Sol. Energy Mater. Sol. Cells 153 (2016) 31–43.
[9] J.D. Murphy, R.E. McGuire, K. Bothe, V.V. Voronkov, R.J. Falster, Minority carrier lifetime in silicon photovoltaics: the effect of oxygen precipitation, Sol. Energy Mater. Sol. Cells 120 (2014) 402–411.
[10] J.D. Murphy, M. Al-Amin, K. Bothe, M. Olmo, V.V. Voronkov, R.J. Falster, The effect of oxide precipitates on minority carrier lifetime in n-type silicon, J. Appl. Phys. 118 (2015) 215706.
[11] J. Haunschild, I.E. Reis, J. Geilker, S. Rein, Detecting efficiency-limiting defects in Czochralski-grown silicon wafers in solar cell production using photoluminescence imaging, Phys. Status Solidi RRL 5 (5–6) (2011) 199–201.
[12] F. Jay, B. Martel, M. Tomassini, R. Peyronnet-Dremière, J. Stadler1, J. Veirman, X. Brun, D. Muñoz, High quality thermal donor doped Czochralski silicon ingot for industrial heterojunction solar cells, in:, Proceedings of the 31st European Photovoltaic Solar Energy Conference and Exhibition, 2015, pp. 316–321.
[13] E. Letty, J. Veirman, W. Favre, M. Lemiti, Bulk defect formation under light soaking in seed-end n-type Czochralski silicon wafers – effect on silicon heterojunction solar cells, Sol. Energy Mater. Sol. Cells 166 (2017) 147–156.
[14] R. Søndena, Y. Hu, M. Juel, M. Syre Wiig, H. Angelskar, Characterization of the OSF-band structure in n-type Cz-Si using photoluminescence-imaging and visual inspection, J. Cryst. Growth 367 (2013) 68–72.
[15] J. Veirman, B. Martel, N. Enjalbert, S. Dubois, C. Picoulet, P. Bonnard, Oxygen-defect characterization for improving R&D relevance and Cz-Si solar cell efficiency, Photovolt. Int. 33 (2016).
[16] T. Trupke, B. Mitchell, J.W. Weber, W. McMillan, R.A. Bardos, R. Kroeze, Photoluminescence imaging for photovoltaic applications, Energy Procedia 15 (2012) 135–146.
[17] M. Wilson, Jacek Lagowski, Piotr Edelman, Ferenc Korsos, Gyorgy Nadudvari, Zoltan Kiss, Joerg Schmauder, Valentin Mihailetchi, Sara Olibet, Unified lifetime metrology and photoluminescence imaging, Energy Procedia 38 (2013) 209–215.
[18] Andrew Findlay, Jacek Lagowski, Marshall Wilson, John D'Amico1, Alexandre Savtchouk1, Ferenc Korsos, Gyorgy Nadudvari, Inline PL inspection and advanced offline evaluation of passivation defects, charge and interfaces, Solid State Phenom. 205–206 (2014) 128–135.
[19] J. Donecker, M. Naumann, Laser scattering tomography for crystal characterization: quantitative approaches, Cryst. Res. Technol. 37 (2002) 147–157.
[20] T. Desrues, S. Gall, C. Lorfeuvre, S. Manuel, R. Monna, Y. Veschetti, Understanding the recombination activity of diffused boron emitters for high efficiency n-type solar cells, in: Proceedings of the the 31st European Photovoltaic Solar Energy Conference and Exhibition, 2015, pp 991–993.
[21] G. Paráda, F. Korsós, P. Tüttő, Transient method for lifetime characterization of monocrystalline Si ingots, in: Proceedings of the 29th European Photovoltaic Solar Energy Conference and Exhibition, 2013, pp. 1264–1266.
[22] M. Wilson, P. Edelman, J. Lagowski, S. Olibet, V. Mihailetchi, Improved QSS-μPCD measurement with quality of decay control: correlation with steady-state carrier lifetime, Sol. Energy Mater. Sol. Cells 106 (2012) 66–70.
[23] M. Tomassini, J. Veirman, R. Varache, E. Letty, S. Dubois, Y. Hu, Ø. Nielsen, Recombination activity associated with thermal donor generation in monocrystalline silicon and effect on the conversion efficiency of heterojunction solar cells, J. Appl. Phys. 119 (2016) 084508.
[24] H. Steinkemper, M. Hermle, S.W. Glunz, Comprehensive simulation study of industrially relevant silicon solar cell architectures for an optimal material parameter choice, Prog. Photovolt.: Res. Appl. 24 (2016) 1319–1331.